

NASA Contractor Report 201594

ICASE Report No. 96-51

ICASE

QUADRATURE-FREE IMPLEMENTATION OF DISCONTINUOUS GALERKIN METHOD FOR HYPERBOLIC EQUATIONS

H. L. Atkins
Chi-Wang Shu

NASA Contract No. NAS1-19480
August 1996

Institute for Computer Applications in Science and Engineering
NASA Langley Research Center
Hampton, VA 23681-0001

Operated by Universities Space Research Association



*National Aeronautics and
Space Administration*

Langley Research Center
Hampton, Virginia 23681-0001

QUADRATURE-FREE IMPLEMENTATION OF DISCONTINUOUS GALERKIN METHOD FOR HYPERBOLIC EQUATIONS

H. L. Atkins¹

Aerodynamic and Acoustic Methods Branch
NASA Langley Research Center
Hampton, VA 23681-0001

Chi-Wang Shu²

Division of Applied Mathematics
Brown University
Providence, RI 02912

ABSTRACT

A discontinuous Galerkin formulation that avoids the use of discrete quadrature formulas is described and applied to linear and nonlinear test problems in one and two space dimensions. This approach requires less computational time and storage than conventional implementations but preserves the compactness and robustness inherent in the discontinuous Galerkin method. Test problems include the linear and nonlinear one-dimensional scalar advection of both smooth and discontinuous initial value problems, the two-dimensional scalar advection of smooth initial value problems that are discretized by using unstructured grids with varying degrees of smoothness and regularity, and two-dimensional linear Euler solutions on unstructured grids.

¹Research Scientist, National Aeronautics and Space Administration.

²Professor, Research supported by NASA Contract NAS1-19480 while this author was in residence at ICASE, NASA Langley Research Center, Hampton, VA 23681-0001, and by NASA Grant NAG-1-1145, ARO Grant DAAH04-94-G-0205, NSF Grant DMS-9500814, and AFOSR Grant 95-1-0074.

Introduction

Computational methods for aeroacoustics must possess accuracy properties that exceed those of conventional second-order computational fluid dynamics (CFD) methods. At the same time, many problems of interest involve complex geometries that are not easily treated by common high-order methods that normally require a smooth, structured grid. In addition to the geometrically complex problem, we are particularly interested in strongly nonlinear flows that contain shock waves as a major source of sound generation, such as in the case of jet noise.

In an effort to satisfy these requirements, the relatively untried discontinuous Galerkin (DG) method is being tested for hyperbolic problems. Some advantages of this approach include the ease with which the method can be applied to both structured and unstructured grids and its suitability for parallel computer architectures. This approach also has several useful mathematical properties.

Johnson and Pitkäranta¹ proved stability and error estimates for linear scalar advection. In a series of papers, Cockburn et al.²⁻⁴ discussed the DG method with the use of approximate Riemann solvers, limiters, and total-variation diminishing (TVD) Runge-Kutta time discretizations for nonlinear hyperbolic problems. In reference 2, the general formulation in one space dimension is provided; This work includes an analysis of the accuracy and stability (in terms of total variation) and a detailed description of the implementation. Numerical examples using the scalar equations are also provided. In reference 3, the method is applied to one-dimensional systems. Stability of the initial boundary value problem for a linear system is proved, and numerical experiments are presented for the one-dimensional Euler equations. In reference 4, the method is generalized to multispace dimensions. A main result in reference 4 is the design of a limiter that applies to general triangulations, maintains a high order of accuracy in smooth regions, and guarantees maximum norm stability. Jiang and Shu⁵ have also proved that the DG method satisfies a local cell entropy inequality for the square entropy, for arbitrary triangulations

in any space dimension, and for any order of accuracy. This proof trivially implies L_2 stability of the method for nonlinear shocked problems in the scalar case.

Although the DG method has not been widely used in the CFD arena, several instances exist in which this method has been applied to the Euler or Navier-Stokes equations.^{3,4,6-9} Halt and Agarwal⁶ applied the method of moments (similar to the DG method) to the steady, two-dimensional Euler equations for subsonic flows. Bassi and Rebay⁷ applied the DG method to two-dimensional Euler equations for transonic flows and demonstrated the importance of the proper treatment of curved boundaries. In reference 8, Bassi and Rebay extended their method to the Navier-Stokes equations by introducing the gradient of the solution as an auxiliary variable. Most recently, Lowrie, Roe, and van Leer⁹ presented a fully discrete DG method for the unsteady Euler equations. Biswas, Devine, and Flaherty¹⁰ applied the DG method in an h-p version in an adaptive grid environment and considered the issues in using limiters for moments, as well as for parallel implementations.

In the works described above, the integrals that appear in the formulation are evaluated with quadrature formulas. In this particular work, the DG method is implemented in a form that avoids the use of quadrature formulas with the goal of improving the efficiency of the method. In the first section, the DG method is described in general. Then, additional motivation for using the quadrature-free approach is given, along with specific details of the formulation. Storage requirements and operation count are also discussed, and the results of a stability analysis are given. It is shown that the primary arguments against the method, high storage requirements and a high operation count, are unjustified. The last section presents numerical results for one- and two-dimensional test problems. A linear scalar equation is used to verify the general properties of the DG method for solution expansions up to degree 12. The nonlinear Burgers' equation is used to demonstrate the shock-capturing capabilities of the method in one space dimension. The method is applied to both scalar advection and the linear Euler equations in two space dimensions

to demonstrate the unstructured grid capability. This work focuses on the new formulation of the DG method and defers all discussion of boundary conditions to future articles. Hence, all test problems are treated as spatially periodic.

General Discontinuous Galerkin Method

Consider an arbitrary domain Ω in which the solution is governed by a conservation equation of the form

$$U_t + \nabla \cdot \vec{F} = 0 \quad (1)$$

The DG method can be obtained by partitioning the domain onto smaller, nonoverlapping elements Ω_i that cover the domain and then applying a traditional Galerkin¹¹ method to each element. The Galerkin approach within an element is defined by selecting a finite-dimensional basis set, approximating the solution as an expansion in that basis, and then projecting the governing equation onto each member of that basis set:

$$B \equiv \{b_k, 0 \leq k \leq N(p, d)\} \quad (2)$$

$$U_{\Omega_i} \approx V_i \equiv \sum_{j=0}^N v_{i,j} b_j \quad (3)$$

$$\int_{\Omega_i} b_k \left(V_t + \nabla \cdot \vec{F} \right)_i d\Omega = 0 \quad (0 \leq k \leq N, 0 < i \leq I) \quad (4)$$

where I is the total number of elements. The basis set must be constructed from the lower order terms of a complete and linearly independent set. In the fully discrete approach,⁹ the basis set contains both temporal and spatial functions. In the semidiscrete approach, which is used here, the basis set contains only spatial functions, and the solution expansion coefficients $v_{i,j}$ are functions of time. The number of terms in the expansion, $N(p, d) + 1$, depends on the degree of the expansion p and the number of time-space dimensions d that are represented. When the basis functions are polynomials of degree p , Johnson et al.¹ proved the order of accuracy of the

method to be at least $p+1/2$. In practice, however, the order of accuracy of the method observed in most cases is $p+1$. Except where the full form is needed for clarity, $N(p, d)$ will be denoted simply by N to streamline the notation.

The divergence term is recast by applying integration by parts as

$$\int_{\Omega_i} b_k \sum_{j=0}^N (v_{i,j})_t b_j d\Omega - \int_{\Omega_i} \nabla b_k \cdot \vec{F}_i d\Omega + \int_{\partial\Omega_i} b_k \vec{F}_i^R \cdot d\vec{s} = 0 \quad (0 \leq k \leq N, 0 < i \leq I) \quad (5)$$

where $d\vec{s}$ is an outward-pointing surface-element normal and the flux vector \vec{F}^R is some approximation to a Riemann flux that depends on the solutions in both element i and the neighboring element. The approximate Riemann flux provides the crucial coupling between elements as well as the correct upwind bias required to ensure stability.

Although equation (5) could be evaluated in physical space, the equation can be conveniently (and sometimes advantageously) represented in terms of coordinates that are local to the element. After such a mapping, equation (5) becomes

$$\int_{\Omega_i} b_k \sum_{j=0}^N (v_{i,j})_t b_j J_i d\Omega - \int_{\Omega_i} \nabla b_k \cdot \mathbf{J}_i^{-1} \vec{F}_i J_i d\Omega + \int_{\partial\Omega_i} b_k \mathbf{J}_i^{-1} \vec{F}_i^R \cdot J_i d\vec{s} = 0 \quad (0 \leq k \leq N, 0 < i \leq I) \quad (6)$$

where

$$\mathbf{J}_i \equiv \frac{\partial(x, y, z)}{\partial(\xi, \eta, \zeta)}, \quad J_i = |\mathbf{J}_i|$$

and (ξ, η, ζ) are the local coordinates within the element.

Depending on the choice of basis functions and the form of J_i , the first integral can usually be simplified. If, for example, the basis set is orthonormal with respect to J_i , then the first integral term in equation (6) reduces to an identity mass matrix. In most implementations, either

the transformation is an isoparametric form (thus, J_i is a polynomial) or the element is allowed to be an arbitrary polygon. In either case, the temporal term can be expressed as $\mathbf{M}_i \mathbf{V}_t$, where $\mathbf{M}_i \equiv [m_{k,j}]$ is the mass matrix, $\mathbf{V} \equiv [v_l]$, and

$$m_{k,j} = \int_{\Omega_i} b_k b_j J_i d\Omega \quad (7)$$

In most cases, the mass matrix can be computed and inverted in advance of the main calculation; however, it must be stored for every element. In all previous implementations, the spatial integrals are evaluated with quadrature formulas that are appropriate to the element shape and the required degree of accuracy. The resulting $N + 1$ equations are then used to temporally evolve the coefficients of the solution expansion $v_{i,j}$.

In the present formulation, we place a fundamental restriction on the types of elements that are permitted. In particular, we require that all elements (except perhaps elements near a curved boundary) have a linear mapping to a simple similarity element, such as an equilateral triangle or a square in two dimensions (or other simple elements in three dimensions). With this restriction, the temporal term can be rewritten as $J_i \mathbf{M} \mathbf{V}_t$, where the mass matrix \mathbf{M} is now defined by

$$m_{k,j} = \int_{\Omega} b_k b_j d\Omega \quad (8)$$

As a consequence, \mathbf{M} is the same for all elements of a given similarity shape (e.g., one \mathbf{M} is applicable to all triangles, another is applicable to all squares, and so on) except those near a curved boundary. The considerable reduction in the amount of storage needed far outweighs the inconvenience that may arise from the restriction in element shape.

Throughout the remainder of this discussion, the subscript that identifies the element will be omitted unless its use is necessary for clarity. In addition, although the above discussion applies to a general basis set, the remaining discussion will assume that the basis functions are polynomials. In particular, the results presented later use a basis that is constructed from simple monomials (e.g., $B \equiv \{1, x, y, x^2, xy, y^2, \dots\}$).

Quadrature-Free Approach

Quadrature formulas, especially Gaussian quadrature formulas, are usually the most accurate and efficient means of evaluating integrals. However, this feature is based on the assumption that the data are readily available at the quadrature points (i.e., the data are stored there), which is typical for most finite-element and spectral-element methods. In these methods, the unknown variables are the values of the solution at the quadrature points, and the basis or “shape” functions are often the Lagrangian polynomials associated with the quadrature points. In the DG method, however, the formulation requires the evaluation of both volume and surface integrals, and no single set of $N + 1$ quadrature points exists that can be used to evaluate all integrals to the required accuracy. Thus, the usual practice in the implementation of the DG method is to choose a basis and store the expansion coefficients. As a consequence, the evaluation of the volume integral, for example, requires $N + 1$ operations at each quadrature point simply to obtain the data needed to evaluate the quadrature formula. Because all integrals must be exact for polynomials of degree $2p$, the operation count for the complete evaluation of the volume integral is on the order of 2 to 3 times $N + 1$ operations for each equation, with the assumption that optimal quadrature formulas exist.

In contrast, if the basis functions are judiciously chosen such that integrals of products of the basis functions can be evaluated exactly, then the complete volume integral can be evaluated exactly in $N + 1$ or fewer operations. A more precise comparison of the operation count is given in a later section. In the quadrature-free implementation, we derive a set of matrices that accomplish this task. Further, as a consequence of the restriction previously placed on the element type, these matrices are the same for all elements of a given type (i.e., one set of matrices applies to all triangles, another set applies to all squares, and so on). The result is a method with low storage requirements and low computational cost that retains the ability to treat unstructured grids in an accurate and robust manner.

Flux Expansion

To accomplish this task, however, an efficient method for expanding the flux vector \vec{F} in terms of the basis set is needed:

$$\vec{F} = \sum_{j=0}^M \vec{f}_j b_j \quad M \geq N(p, d) \quad (9)$$

where the number of terms in the expansion M depends on the form of the nonlinearity in \vec{F} . To obtain the design order of accuracy, M must be at least as large as $N(p+1, d)$, such that the degree of $\nabla b_k \cdot \vec{F}$ is at least as large as the degree of $b_k V$.

The expansion is trivially accomplished when \vec{F} is a linear function of U . In this case, the coefficients \vec{f}_j are identically zero for $j > N(p, d)$. Similarly, for common test problems such as the nonlinear Burgers' equation, $\vec{F} = \frac{1}{2} U(x)^2$ can be obtained by multiplication so long as triple (and higher) products of the basis function are also easily integrated. Such is the case when the basis functions are polynomials in the local coordinates of a simple element.

The more complex flux functions, such as those of the Euler equations, can be treated in several ways. One approach is that of Lowrie et al.,⁹ in which the solution expansion is applied to the parameter vector $[\sqrt{\rho}, \sqrt{\rho}u, \sqrt{\rho}v, \sqrt{\rho}H]$ rather than the conserved variables $[\rho, \rho u, \rho v, \rho e]$. Although this approach allows all nonlinear fluxes to be evaluated exactly, the coefficient matrices become dependent on the local solution. Hence, the coefficient matrices derived here would be different for every element and would need to be recomputed at every time step; as a result, the storage requirements and computational effort would be unacceptably high.

A general alternative is to expand the flux in a Taylor series. Because the Euler equations consist of terms such as $(\rho u)^2/\rho$ and $(\rho u)(\rho v)/\rho$, a practical procedure is to approximate ρ^{-1} in the basis functions by using a Taylor series and then use multiplication to complete the flux expansion.

Another approach is to define the flux in terms of the projection operator as follows. Let

$$\rho^{-1} \approx \bar{\rho} \equiv \sum_{j=0}^M r_j b_j \quad (10)$$

then

$$\rho^{-1} \rho = 1 \Rightarrow \int_{\Omega} b_k \bar{\rho} \rho d\Omega = \int_{\Omega} b_k d\Omega \quad (k = 0, 1, 2, \dots, M) \quad (11)$$

This set of equations results in a system that is linear in r_j and can easily be solved exactly.

The flux terms, such as $(\rho u)(\rho v)/\rho$, can then be computed by multiplication, just as in the Taylor series approach. Alternatively, the projection method can be used to determine the flux expansion directly. Let

$$(\rho u)(\rho v)/\rho \approx F \equiv \sum_{j=0}^M b_j f_j \quad (12)$$

Then,

$$\int_{\Omega} b_k \rho F d\Omega = \int_{\Omega} b_k (\rho u)(\rho v) d\Omega \quad (k = 0, 1, 2, \dots, M) \quad (13)$$

defines a set of equations that is linear for f_j .

The projection approach is appealing because the error of the approximate flux is minimized over the whole of the element, whereas in the Taylor series approach the flux will be more accurate near the center of the element than near the edges of the element.

Volume Integral

After the flux is represented as in equation (9), the volume integral of equation (6) can easily be rewritten as a matrix times a vector as

$$J \mathbf{M} \mathbf{V}_t - \vec{\mathbf{G}} \cdot \vec{\mathbf{F}} + \int_{\partial\Omega} \mathbf{B} \mathbf{J}^{-1} \vec{F}^R \cdot J d\vec{s} = 0 \quad (14)$$

where $\mathbf{V} = [v_k]$, $\vec{\mathbf{G}} = [\vec{g}_{k,j}]$, $\vec{\mathbf{F}} = [\vec{f}_j]$, $\mathbf{B} = [b_k]$,

$$\begin{aligned} \vec{g}_{k,j} &= \int_{\Omega} (\nabla b_k) b_j d\Omega, & \vec{f}_j &= J \mathbf{J}^{-1} \vec{f}_j \\ (k &= 0, 1, 2, \dots, N; \quad j = 0, 1, 2, \dots, M) \end{aligned} \quad (15)$$

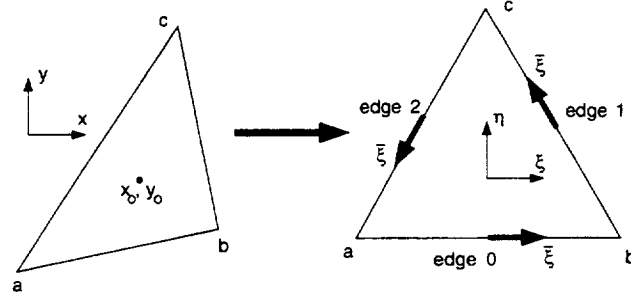
and $M \geq N$ depends on the degree to which a nonlinear flux must be expanded. The vector matrix \vec{G} is a constant for all elements of a given family and can be precomputed and stored. The evaluation of the volume integral becomes an order $M + 1$ operation for each of the $N + 1$ equations in the element.

Boundary Integral

The boundary integral is partitioned into segments associated with the sides of the element. The integral on each boundary segment can be rewritten in terms of a vector times a precomputed matrix; however, the procedure is complicated by the fact that \vec{F}^R is a function of the solution in the two elements on either side of a boundary segment and each of these elements has a distinct local coordinate system. The remedy is to translate each basis function from its local coordinate system to a coordinate system that is common to both elements. The use of a boundary-segment-based coordinate system actually results in a reduction in the total work and storage required. The complete process can be summarized in three steps: translate the solution to an edge coordinate system, compute the approximate Riemann flux in the edge coordinates, and project the flux onto the space defined by the element basis set.

For clarity, the procedure is illustrated for a triangular element; however, the same procedure can be applied to all element types, and the procedure facilitates the use of mixed element types (i.e., squares and triangles together). Figure 1 illustrates a general triangle that has been mapped into an equilateral triangle. The equilateral triangle has a local coordinate system (ξ, η) with its origin at the centroid of the element; each edge also has a local coordinate $\bar{\xi}$ with its origin in the center of the edge. Note that the dimensionality of the edge coordinate system is lower than that of the element by 1.

For each edge of the triangle, a constant matrix T_j exists that relates each member of the local basis to an expansion in terms of the edge coordinate. The subscript j identifies the edge



$$\begin{bmatrix} x - x_o \\ y - y_o \end{bmatrix} = \mathbf{J} \begin{bmatrix} \xi \\ \eta \end{bmatrix}$$

Figure 1. Transform from general triangle to equilateral similarity triangle that shows coordinate systems associated with interior and edges of similarity triangle. to which the matrix applies. For example, on edge 0,

$$\mathbf{B} \equiv [b_l] = \begin{bmatrix} 1 \\ \xi \\ \eta \\ \xi^2 \\ \xi\eta \\ \eta^2 \\ \vdots \end{bmatrix} = \begin{bmatrix} 1 & 0 & 0 & \dots \\ 0 & 1 & 0 & \dots \\ \frac{-1}{2\sqrt{3}} & 0 & 0 & \dots \\ 0 & 0 & 1 & \dots \\ 0 & \frac{-1}{2\sqrt{3}} & 0 & \dots \\ \frac{1}{12} & 0 & 0 & \dots \\ \vdots & \vdots & \vdots & \ddots \end{bmatrix} \begin{bmatrix} 1 \\ \bar{\xi} \\ \bar{\xi}^2 \\ \vdots \end{bmatrix} = \mathbf{T}_0 [\bar{b}_j] \equiv \mathbf{T}_0 \bar{\mathbf{B}} \quad (16)$$

The matrices for the other two edges are considerably more dense but are easily derived in exact form with the aid of a symbolic algebra package such as Maple or Mathematica. The \mathbf{T}_j matrix for square elements is relatively sparse on all four edges.

Given any function that is expanded in terms of the element basis, the expansion in terms of the edge basis $\bar{\mathbf{B}}$ is derived as follows:

$$V_i = \sum_{j=0}^N v_{i,j} b_j = \mathbf{V}_i^T \mathbf{B} = \mathbf{V}_i^T \mathbf{T}_j \bar{\mathbf{B}} = [\mathbf{V}_i^T \mathbf{T}_j^T]^T \bar{\mathbf{B}} \equiv \bar{\mathbf{V}}_{i,j}^T \bar{\mathbf{B}} \quad (17)$$

hence,

$$\bar{\mathbf{V}}_{i,j} = \mathbf{T}_j^T \mathbf{V}_i \quad (18)$$

After $\bar{\mathbf{V}}_{i,j}$ has been computed on every face of every element, the flux through an edge can be computed without regard to the type of elements or the orientation of the coordinate

system of the elements that border the edge. At an arbitrary edge, illustrated in Figure 2, we arbitrarily designate one element to be on the left and the other to be on the right. The two edge

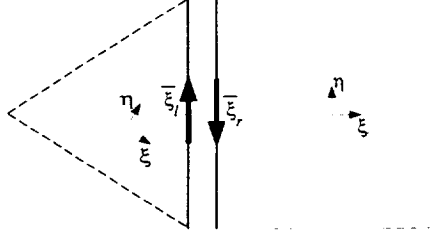


Figure 2. Relation of edge coordinates of adjacent elements.

coordinate systems of the two elements always point in opposite directions. A function of the edge coordinates of the right element can be represented in terms of the edge coordinate system of the left element simply by negating the odd members of $\bar{\mathbf{V}}_{i,j}$. In the three-dimensional case, the relation is not as trivial because a rotation may also be involved.

In the present work, the Riemann flux is approximated by a simple Lax-Friedrichs flux of the form

$$J \mathbf{J}^{-1} \vec{F}_l^R \cdot d\vec{s} \equiv \frac{1}{2} \left\{ \left[J \mathbf{J}^{-1} (\vec{F}_l + \vec{F}_r) \right] \cdot \vec{n} - \alpha (V_r - V_l) \right\} ds \quad (19)$$

where $d\vec{s} = \vec{n} ds$, the subscripts l and r denote the left and right sides of the edge, \vec{n} points from left to right, and α is some smooth positive function that is greater in magnitude than the eigenvalues of the Jacobian of $\frac{1}{2} \left[J \mathbf{J}^{-1} (\vec{F}_l + \vec{F}_r) \right] \cdot \vec{n}$. By applying equation (18), the Lax-Friedrichs flux is easily expressed in terms of the edge coordinate to give

$$J \mathbf{J}^{-1} \vec{F}_l^R \cdot d\vec{s} = \bar{\mathbf{F}}_l^T \bar{\mathbf{B}} ds \quad (20)$$

where

$$\begin{aligned} \bar{\mathbf{F}}_l &\equiv [\bar{f}_0, \bar{f}_{,1}, \bar{f}_{,2}, \bar{f}_{,3} \dots] \\ &= \left\{ \left[J \mathbf{J}^{-1} (\mathbf{T}_{j_l} \bar{\mathbf{F}}_l + \hat{\mathbf{I}} \mathbf{T}_{j_r} \bar{\mathbf{F}}_r) \right] \cdot \vec{n} - \alpha (\hat{\mathbf{I}} \mathbf{T}_{j_r} \mathbf{V}_r - \mathbf{T}_{j_l} \mathbf{V}_l) \right\} / 2 \\ &= \left\{ \left[J \mathbf{J}^{-1} (\bar{\mathbf{F}}_l + \hat{\mathbf{I}} \bar{\mathbf{F}}_r) \right] \cdot \vec{n} - \alpha (\hat{\mathbf{I}} \bar{\mathbf{V}}_r - \bar{\mathbf{V}}_l) \right\} / 2 \end{aligned} \quad (21)$$

and $\hat{\mathbf{I}} = \text{diag}(1, -1, 1, -1, \dots)$ accounts for the difference in the left and right edge coordinates. The coefficients of the approximate Riemann flux on the right face are simply $\bar{\mathbf{F}}_r = \hat{\mathbf{I}}^{-1} \bar{\mathbf{F}}_l$. As a side note, depending on the form of the flux, less computational effort may be required to compute $\bar{\mathbf{F}}$ directly from $\bar{\mathbf{V}}$ than to translate the flux from element to edge coordinates, particularly for linear fluxes.

Finally, the boundary integral is evaluated in the edge frame of reference by expressing b_k in terms of the edge coordinates and collecting in terms of the components of $\bar{\mathbf{F}} = [\bar{f}_0, \bar{f}_1, \bar{f}_2, \dots]$. To illustrate, let $[t_k]_j$ denote the k th row of \mathbf{T}_j . The integral on a boundary segment becomes

$$\begin{aligned}
\int_{\partial\Omega} (b_k)(\bar{\mathbf{F}}^T \bar{\mathbf{B}}) ds &= \int_{\partial\Omega} ([t_k]_j \bar{\mathbf{B}})(\bar{\mathbf{F}}^T \bar{\mathbf{B}}) ds \\
&= \int_{\partial\Omega} [(t_{k,0} + t_{k,1}\bar{\xi} + t_{k,2}\bar{\xi}^2 + t_{k,3}\bar{\xi}^3 + \dots) \cdot (\bar{f}_0 + \bar{f}_1\bar{\xi} + \bar{f}_2\bar{\xi}^2 + \bar{f}_3\bar{\xi}^3 + \dots)] ds \\
&= \int_{\partial\Omega} [(t_{k,0} + t_{k,1}\bar{\xi} + t_{k,2}\bar{\xi}^2 + \dots)\bar{f}_0 + (t_{k,0}\bar{\xi} + t_{k,1}\bar{\xi}^2 + t_{k,2}\bar{\xi}^3 + \dots)\bar{f}_1 \\
&\quad + (t_{k,0}\bar{\xi}^2 + t_{k,1}\bar{\xi}^3 + t_{k,2}\bar{\xi}^4 + \dots)\bar{f}_2 \dots] ds \\
&\equiv [e_k] \bar{\mathbf{F}}
\end{aligned} \tag{22}$$

where $[e_k]$ is a constant row matrix that is easily evaluated exactly. Let \mathbf{E} denote the matrix that is generated by applying the above process to each member of the basis set. The final form of the semidiscrete equation is

$$\mathbf{V}_t - \mathbf{J}^{-1} \left[\mathbf{M}^{-1} \vec{\mathbf{G}} \cdot \bar{\mathbf{F}} - \sum_{k=1}^{n_e} (\mathbf{M}^{-1} \mathbf{E}_k \bar{\mathbf{F}}_k) \right] = 0 \tag{23}$$

where n_e is the number of edges and the matrices $\mathbf{M}^{-1} \vec{\mathbf{G}}$ and $\mathbf{M}^{-1} \mathbf{E}_k$ are constant matrices that apply to all elements of a given type. Furthermore, these matrices can be efficiently precomputed by the procedure just described.

Computational Effort

The effort required to evaluate the complete spatial operator is contained in three basic operations: the evaluation of equation (23) for each element, the evaluation of equation (18) for each edge of each element, and the computation of $\vec{\mathbf{F}}$ and $\bar{\mathbf{F}}$ from \mathbf{V} and $\bar{\mathbf{V}}$, respectively. The operation count of the first two operations is directly related to the size of the matrices $\mathbf{M}^{-1}\vec{\mathbf{G}}$, $\mathbf{M}^{-1}\mathbf{E}_k$, and \mathbf{T}_j . The row dimension of all three matrices is $N(p, d) + 1$. If the flux is linear, then the column space of $\mathbf{M}^{-1}\vec{\mathbf{G}}$ is also $N(p, d) + 1$. However, in the nonlinear case the flux must be expanded to at least degree $p + 1$; thus, the column dimension must be at least $N(p + 1, d) + 1$. The column dimension of both $\mathbf{M}^{-1}\mathbf{E}_k$ and \mathbf{T}_j is $N(p, d - 1) + 1$.

The operation count of the flux computation can vary considerably, depending on the complexity of the flux function. In the linear case, the operation count is on the order of $N(p, d) + 1$ and $N(p, d - 1) + 1$ for $\vec{\mathbf{F}}$ and $\bar{\mathbf{F}}$, respectively. The operation count in the nonlinear case could be as high as $[N(p, d) + 1][N(p + 1, d) + 1]$ and $[N(p, d - 1) + 1]^2$ for $\vec{\mathbf{F}}$ and $\bar{\mathbf{F}}$, respectively. Thus, the total operation count for the spatial operator in a single element varies from

$$\begin{aligned} & d[N(p, d) + 1]^2 + 2n_e[N(p, d) + 1][N(p, d - 1) + 1] \\ & + O\{d[N(p, d) + 1] + n_e[N(p, d - 1) + 1]\} \end{aligned} \quad (24)$$

for the linear case to

$$\begin{aligned} & d[N(p, d) + 1][N(p + 1, d) + 1] + 2n_e[N(p, d) + 1][N(p, d - 1) + 1] \\ & + O\{d[N(p + 1, d) + 1][N(p, d - 1) + 1] + n_e[N(p, d - 1) + 1]^2\} \end{aligned} \quad (25)$$

for the nonlinear case. For these estimates the matrices are assumed to be full, which is not the case. The exact form of $N(p, d)$ is

$$N(p, d) = dp + \begin{cases} 0 & d = 1 \\ p(p - 1)/2 & d = 2 \\ 3p(p - 1)/2 & d = 3 \\ 3p(p - 1) & d = 4 \end{cases} \quad (26)$$

and Table 1 gives $N(p, d) + 1$ for $1 \leq p \leq 6$ and for $1 \leq d \leq 4$.

In a conventional DG implementation (i.e., one that uses quadrature points), the operation count is on the order of

$$[N(p, d) + 1][(1 + d)N_{qv} + 2n_e N_{qb}] + O(dN_{qv} + n_e N_{qb}) \quad (27)$$

where N_{qv} and N_{qb} denote the number of quadrature points required for the volume integral and boundary segment integrals, respectively, and the last term denotes the cost of computing the flux at each quadrature point. Most references do not give the specific quadrature formulas used; however, Halt et al.⁶ referred to the work of Dunavant,¹² who derived nearly optimal formulas in which $N_{qv} > N(p, d) + 1$ in order to evaluate the integral exactly to degree $2p$. Thus, the operation count for the conventional DG implementation is greater than the values given by either (26) or (27) regardless of whether we take advantage of the sparseness of the matrices.

When the DG method is compared with fundamentally different methods such as finite-difference or finite-volume methods, the comparison must be done in an equitable manner. To do so, we hypothesize that any two methods with the same order of accuracy and the same physical stencil size will yield similar results (for benign cases that do not violate the basic assumptions of the method). In practice, we compare methods that are of the same order of accuracy and have the same total number of dependent variables. In this frame of reference, the evaluation of the spatial operator is an operation of order $N(p, d) + 1$ or $N(p + 1, d) + 1$ per dependent variable for a linear or nonlinear problem, respectively.

Time Integration and Stability

The solution is advanced in time with a three-stage TVD Runge-Kutta method:¹³

$$\begin{aligned} W^0 &= V^{n-1} \\ W^k &= \beta_k W^0 + (1 - \beta_k) \left[W^{k-1} + \Delta t R(W^{k-1}) \right] \quad k = 1, 2, 3 \\ V^n &= W^3 \end{aligned} \quad (28)$$

where $\beta_k = 0, 3/4$, and $1/3$ for $k = 1, 2$, and 3 , respectively.

Fourier stability analysis has been applied to a generalized K -stage form of equation (28) (i.e., $k = 1, 2, \dots, K$) for the one-dimensional linear case of

$$U_t + a U_x = 0 \quad (29)$$

to determine the stability limit $\lambda_K \equiv a \Delta t / \Delta x$. Results are given in Table 2 for $K = 1, 2$, and 3 and for $0 \leq p \leq 11$. The rapid drop in the stability limit as the order of the method is increased would normally be alarming in comparison with stability constraints of explicit finite-difference methods. However, if we again require that comparisons be made among methods that have the same total number of variables, then the size of the element in the DG method would be larger (by a factor of $p + 1$ in one dimension) than the mesh size of a comparable finite-difference calculation. Thus, most of the drop in the stability limit can be attributed to the definition of Δx . The last column of Table 2 gives $\lambda_K(p + 1)$, which gives the DG stability limit in a form that facilitates comparison with the stability limit of a finite-difference method.

Results

One-Dimensional Test

The one-dimensional version of this method has been tested on the linear problem

$$U_t + a U_x = 0 \quad (30)$$

and the nonlinear problem

$$U_t + \frac{1}{2}(U^2)_x = 0 \quad (31)$$

on the domain $0 < x < 1$ with periodic boundary conditions.

A linear problem is solved first with smooth initial conditions $U(0, x) = \frac{1}{2} + \sin(2\pi x)$ to demonstrate the general accuracy properties of the method. The numerical solution is initialized by expanding the initial condition in a Taylor series about the center of each element. All

components of the numerical solution are compared with the Taylor series of the exact solution after it has advected for several periods. The L_n error of the j th component of the solution is defined as

$$L_n(\varepsilon_j) \equiv \left[\left(\sum_{i=1}^I |v_{i,j} - u_{i,j}|^n \right) / I \right]^{1/n}$$

where $u_{i,j}$ denotes the Taylor coefficient of the exact solution in cell i and I denotes the number of elements. A mesh-refinement study has been performed for $p = 1$ through 5. The time step was chosen to be sufficiently small such that the error would be dominated by the spatial operator; however, for $p > 2$ the time step varied as $\Delta t \propto (\Delta x)^{(p+1)/3}$ so that the temporal accuracy would be of the same order as the spatial accuracy. Figure 3 shows the L_1 error for each component of the solution for $p = 1, 2$, and 4. The convergence rate of the solution between any two grids, a and b , is defined by

$$\sigma_n^j \equiv \ln \left\{ \frac{[L_n(\varepsilon_j)]_a}{[L_n(\varepsilon_j)]_b} \right\} / \ln \left(\frac{h_a}{h_b} \right) \quad (33)$$

Table 3 gives the convergence rate between the two finest grids in the refinement sequence. Although most cases converge at the design rate of $p + 1$, the v_0 term of the $p = 1$ case converges at a rate of approximately 3, which is 1 higher than expected. This faster convergence is fortuitous and occurs only because the basis functions are incidentally orthogonal. Because v_1 is only second order and v_2 is undefined, a solution of degree greater than 1 cannot be recovered at any point other than the element center without departing from the Galerkin framework. Furthermore, although v_0 converges faster than the design order, its error is still considerably larger than that of the formally third-order case ($p = 2$).

In the second test case, the DG method is applied to the linear problem with a discontinuous initial solution:

$$U(0, x) = \begin{cases} 1 & \frac{1}{4} < x < \frac{3}{4} \\ 0 & x \leq \frac{1}{4}, \quad x \geq \frac{3}{4} \end{cases} \quad (34)$$

Figures 4 through 8 show several results for this case on a grid with 40 elements. Figures 4, 5, and 6 show the solution after one period for $p = 1, 2$, and 6, respectively. Each method has small overshoots that are confined to the neighborhood of the discontinuity. Similar results were observed for up to $p = 11$ (twelfth order). Figures 7 and 8 also show solutions for $p = 6$ (seventh order), but the solution has advected for 5 and 50 periods, respectively. The overshoots neither grow nor spread in time, which is in sharp contrast to the behavior of more traditional methods. A typical finite-difference approach, for instance, would tend to smear a contact discontinuity over a region that grows linearly in time.

Next, the DG method is applied to a linear test case that was prescribed as part of the ICASE/LaRC Workshop on Benchmark Problems in Computational Aeroacoustics;¹⁴ these results are compared with the finite-difference results described in reference 14. The test case consists of a Gaussian pulse that is advected across a uniform domain. The Gaussian pulse has a half-width of 6 and is initially centered on the origin of a domain that ranges from -20 to 450 . Results are shown in Figure 9 for $p = 1, 2$, and 3; however, as p is increased, the number of elements is decreased such that the total number of variables is approximately 470 (the number of points specified in the workshop). In Figure 10, the results of the fourth-order DG method at $t = 400$ are compared in detail with the results of a fourth- and fifth-order finite-difference method. The results obtained with the fourth-order DG method with only 117 elements is considerably better than that of either the fourth- or the fifth-order finite-difference method with 470 points. (Note that smooth curves are generated for the results obtained with the DG method by evaluating the solution at several points within each element.)

The last one-dimensional test case is a nonlinear problem (eq. (31)) in which a shock forms from an initially smooth solution. This problem was used to not only demonstrate the robustness of the method but also to investigate the effect of truncating the nonlinear flux at various levels. We expect, based on the formulation, that the nonlinear flux must be expanded

to $M = N(p + 1, d)$ terms such that the degree of $\nabla b_k \cdot \vec{F}$ is the same as the degree of $b_k V$ to obtain the design rate of convergence of $p + 1$. This expected convergence property was verified by a mesh-refinement study in which the calculation was stopped just before shock formation. The mesh refinement was performed for several values of p , and the finest grid contained 320 elements. Typical results, shown in Table 4 for $p = 2$, indicate that the convergence rate of the L_∞ error drops to approximately p when $M = N(p, d)$ but is approximately $p + 1$ for all other cases.

Figure 11 shows solutions for $p = 1$ and $p = 2$ (second and third order) in which the shock has formed and has begun to propagate. In both cases, the solutions were obtained without the use of limiters, added dissipation, or entropy correction terms. However, for the case in which $p = 2$ the nonlinear flux needed to be fully expanded ($M = N(2p, d)$); otherwise, the solution diverges shortly after shock formation. All higher order cases ($p > 2$) required some type of limiter. (Research is continuing in this area.)

Two-Dimensional Test

The DG method is applied to the scalar advection equation in two dimensions to demonstrate its robust treatment of unstructured grids. The test problem is given by

$$U_t + a U_x + b U_y = 0 \tag{35}$$

$$U(0, x, y) = [\sin(\pi x) \sin(\pi y)]^4$$

defined on the periodic domain $0 < x, y < 1$. The approximate solution V_i is initialized from the Taylor expansion of the exact initial condition. The baseline case is chosen to be a uniform Cartesian grid that is triangulated in a regular manner, as illustrated in Figure 12. Figure 13 shows the L_1 error in the v_0 component of the solution. As in the one-dimensional case, the time step was small so that the spatial error dominated and for $p > 2$ the time step was proportional to $(\Delta x)^{(p+1)/3}$. In mesh-refinement studies, the first grid in the sequence is coarsened as the order of the method is increased, so that the total number of variables is roughly the same.

The abscissa in Figure 13 is the square root of the total number of variables, which facilitates comparison with a simple fourth-order finite-difference method. The higher order convergence of the $p = 1$ case that was observed in one dimension is not observed in the two-dimensional case. The accuracies of the fourth-order DG and finite-difference methods are quite similar.

One of the major motivations for pursuing a DG method is its ability to maintain accuracy for complex geometries. Here, the baseline grid is altered in several ways to test and demonstrate this capability. Figure 14 illustrates four of the variations that were tested. In the first case, grid A is uniform as in the baseline case, but the triangulation has been performed randomly. In the second case, grid B is generated from grid A by smoothly clustering the grid toward a diagonal. Grid C is generated from grid B by randomly perturbing each grid point by an amount that is less than 20 percent of the average mesh size. In the last case, grid D is generated from the baseline by imposing a piecewise-constant mesh spacing that places half of the points in a narrow band around the axis.

In most cases, the measured error was insensitive to the grid modification or the direction of propagation (i.e., the value of a and b). Figure 15 gives the L_1 error for $p = 3$ (fourth order) on each of the grids shown in Figure 14. Results for other values of p were similar. The results in Figure 15 are for $a = 1$ and $b = 0$ (except for case D2, where $a = 1$ and $b = 1$). The slight increase in error in case D2 is attributed more to the increase in mesh size along the propagation path than to the discontinuous manner in which the mesh size changes.

In the last test case, the DG method is applied to another problem prescribed as part of the ICASE/LaRC Workshop on Benchmark Problems in Computational Aeroacoustics.¹⁴ The linear Euler equations are solved on a square domain of dimensions $-100 < x, y < 100$ with initial conditions that place a compact acoustic source at $x = y = 0$ and a convecting disturbance at $x = 67, y = 0$. Here, the equations have been recast in a form that emphasizes the decoupling

of the convection terms from the acoustic terms that occurs in this linear system:

$$\frac{\partial \mathbf{U}}{\partial t} + \frac{\partial \mathbf{E}}{\partial x} + \frac{\partial \mathbf{F}}{\partial y} = 0 \quad (36)$$

where

$$\mathbf{U} = \begin{bmatrix} \rho - P \\ p \\ u \\ v \end{bmatrix}, \quad \mathbf{F} = \begin{bmatrix} M_x(\rho - P) \\ M_x P + u \\ M_x u + P \\ M_x v \end{bmatrix}, \quad \mathbf{G} = \begin{bmatrix} M_y(\rho - P) \\ M_y P + v \\ M_y u \\ M_y v + P \end{bmatrix}$$

$M_x = 0.5$, $M_y = 0$, and

$$\begin{aligned} (\rho - P)(0, x, y) &= 0.1 \exp \left[(-\ln(2)) \frac{(x - 67)^2 + y^2}{25} \right] \\ P(0, x, y) &= \exp \left[(-\ln(2)) \left(\frac{x^2 + y^2}{9} \right) \right] \\ u(0, x, y) &= 0.04 x P(0, x, y) \\ v(0, x, y) &= 0.04 y P(0, x, y) \end{aligned}$$

The workshop, which targeted finite-difference methods, prescribed a grid of 200×200 . In the present calculation, a uniform $n \times n$ Cartesian grid is used that has been randomly triangulated (as shown in Figure 14(a)) and in which the number of elements is chosen as a function of the degree p such that the total number of unknowns equals approximately 200^2 . Results are shown for $p = 0, 1, 2$, and 3 (first, second, third, and fourth order) with $n = 141, 81, 57$, and 44 , respectively. Figure 16 shows P and u at $t = 40$ for the $p = 3$ case. The wave fronts appear smooth and cylindrical in spite of the fact that the initial disturbance was smaller than the element size. A more quantitative comparison is shown in Figures 17 and 18. The pressure P is plotted on the $x = 0, t = 40$ line for $p = 0$ through 3 at the resolution given above. Also shown is a fine-grid solution with $p = 3$ and $n = 132$ and the solution from a fifth-order finite-difference method on a 200×200 grid. An enlargement of the right peak (Figure 18) shows that all solutions of third-order accuracy or better yield similar results.

Conclusions

A quadrature-free form of the discontinuous Galerkin (DG) method has been formulated for the hyperbolic conservation laws. This approach reduces both the storage and operation count to levels that are comparable to high-order finite-volume methods. The method is well suited to both unstructured and structured grids and has been tested on several one- and two-dimensional problems to demonstrate its accuracy and robustness. On smooth meshes, the accuracy of the DG method is comparable to or better than traditional high-order finite-difference methods. Contact discontinuities are advected without the usual diffusion effect, and nonlinear discontinuities (shocks) are propagated by second- and third-order methods without the use of limiters. On two-dimensional unstructured grids, random and discontinuous mesh variations had little effect on the error and no effect on the convergence of the error.

References

1. C. Johnson and J. Pitkäranta, "An Analysis of the Discontinuous Galerkin Method for a Scalar Hyperbolic Equation," *Mathematics of Computation*, v46 (1986), pp. 1–26.
2. B. Cockburn and C.-W. Shu, "TVB Runge-Kutta local projection discontinuous Galerkin finite element method for conservation laws II: General framework," *Mathematics of Computation*, v52 (1989), pp. 411-435.
3. B. Cockburn, S.Y. Lin, and C.-W. Shu, "TVB Runge-Kutta local projection discontinuous Galerkin finite element method for conservation laws III: One dimensional systems," *Journal of Computational Physics*, v84 (1989), pp. 90-113.
4. B. Cockburn, S. Hou, and C.-W. Shu, "The Runge-Kutta local projection discontinuous Galerkin finite element method for conservation laws IV: The multidimensional case," *Mathematics of Computation*, v54 (1990), pp. 545-581.
5. G. Jiang and C.-W. Shu "On cell entropy inequality for discontinuous Galerkin methods," *Mathematics of Computation*, v62 (1994), pp. 531-538.

6. D. W. Halt and R. K. Agarwal, "Compact Higher Order Characteristic-Based Euler Solver for Unstructured Grids," *AIAA J.*, v30 (1992), pp. 1993–1999.
7. F. Bassi and S. Rebay, "Accurate 2D Euler Computations by means of a High-Order Discontinuous Finite Element Method," *Proceedings of the 14th International Conference on Numerical Methods in Fluid Dynamics*, Bangalor, India, July 11–15, 1994.
8. F. Bassi and S. Rebay, "Discontinuous Finite Element High Order Accurate Numerical Solution of the Compressible Navier-Stokes Equations," Presented at the ICFD Conference on Numerical Methods in Fluid Dynamics, University of Oxford, Oxford, England, April 3–6, 1995.
9. R. B. Lowrie, P. L. Roe, and B. van Leer, "A Space-Time Discontinuous Galerkin Method for the Time-Accurate Numerical Solution of Hyperbolic Conservation Laws," Presented at the 12th AIAA Computational Fluid Dynamics Conference, San Diego, CA, June 19–22, 1995.
10. R. Biswas, K.D. Devine, and J. Flaherty, "Parallel, adaptive finite element methods for conservation laws," *Applied Numerical Mathematics*, v14 (1994), pp. 255–283.
11. C. A. J. Fletcher, *Computational Galerkin Methods* Springer-Verlag, New York, (1984).
12. D. A. Dunavant, "High Degree Efficient Symmetrical Gaussian Quadrature Rules for the Triangle," *International Journal for Numerical Methods in Engineering*, v21 (1985), pp. 119–1148.
13. C.-W. Shu and S. Osher, "Efficient implementation of essentially non-oscillatory shock-capturing schemes," *Journal of Computational Physics*, v77 (1988), pp. 361–383.
14. Harold L. Atkins, "Application of Essentially Nonoscillatory Methods to Aeroacoustic Flow Problems," *Proceedings of ICASE/LaRC Workshop on Benchmark Problems in Computational Aeroacoustics*, Edited by J. C. Hardin, J. R. Ristorcelli, and C. K. W. Tam, NASA CP–3300 (1995), pp. 15–26.

Table 1. $N(p, d) + 1$ for Specific Values of p and d

p	d			
	1	2	3	4
1	2	3	4	5
2	3	6	10	15
3	4	10	19	31
4	5	15	31	53
5	6	21	46	81
6	7	28	64	115

Table 2. $\lambda_K \equiv a \Delta t / \Delta x$ for K -stage Runge-Kutta Methods Applied toDG Method of Degree p (order $p + 1$): \ddagger denotes unstable method

p	λ_1	λ_2	λ_3	$\lambda_3(p + 1)$
0	1.0	1.00	1.256	1.256
1	0.001	0.333	0.409	0.818
2	\ddagger	0.06	0.209	0.627
3	\ddagger	0.02	0.13	0.52
4	\ddagger	0.01	0.089	0.445
5	\ddagger	0.006	0.066	0.396
6	\ddagger	0.004	0.051	0.306
7	\ddagger	0.003	0.04	0.32
8	\ddagger	0.002	0.033	0.297
9	\ddagger	0.002	0.027	0.27
10	\ddagger	0.001	0.023	0.253
11	\ddagger	0.001	0.02	0.24

 \ddagger Unstable method.Table 3. Convergence Rates of $L_1(\varepsilon_j)$ Between Two Finest Grids

p	j				
	0	1	2	3	4
1	2.990	2.133			
2	3.064	3.049	3.022		
4	4.99	5.74	5.00	5.00	5.00

Table 4. Effect of Truncating Nonlinear Flux on Grid Convergence: $p = 2$ case

Convergence Rate	M		
	$N(p, d)$	$N(p + 1, d)$	$N(p + 2, d)$
σ_1^0	2.894	2.944	2.942
σ_∞^0	2.015	2.923	2.921

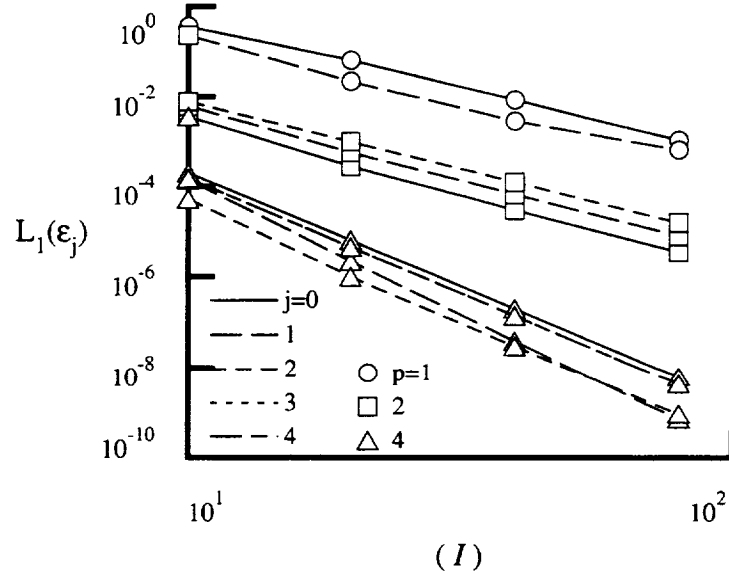


Figure 3. Convergence of L_1 error for $p = 1$, $p = 2$, and $p = 4$.

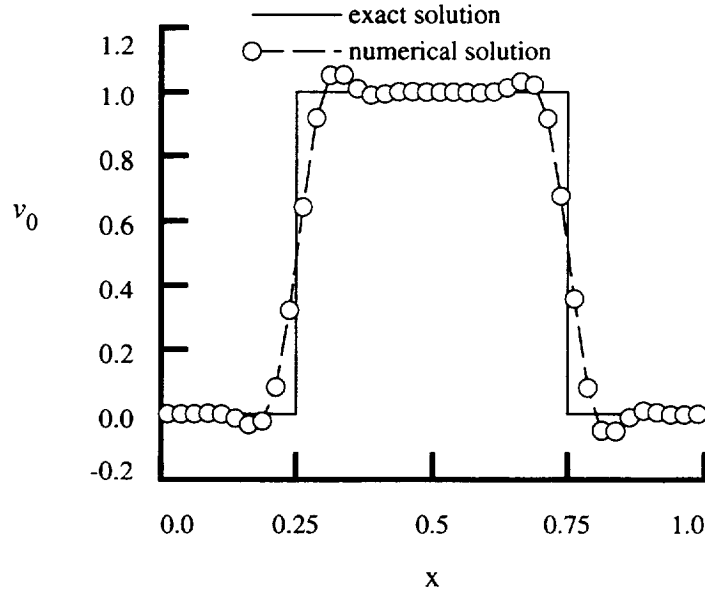


Figure 4. Solution of linear problem after one time period, produced by DG method with $p = 1$.

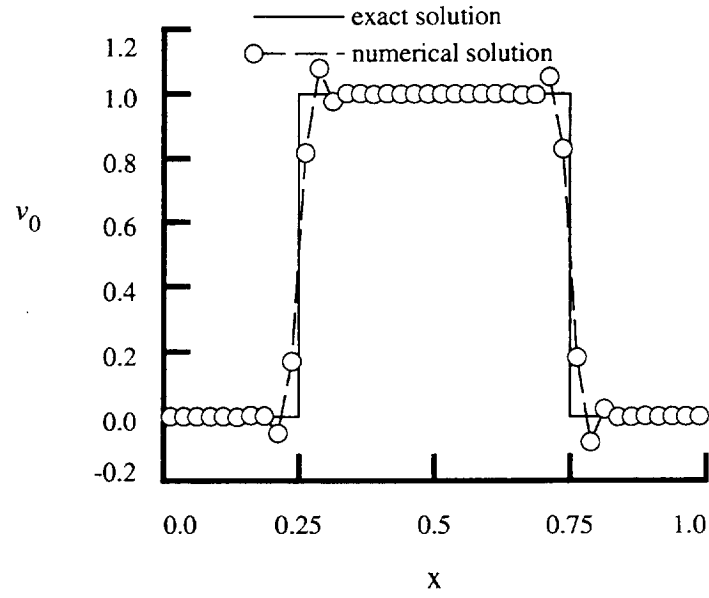


Figure 5. Solution of linear problem after one time period, produced by DG method with $p = 2$.

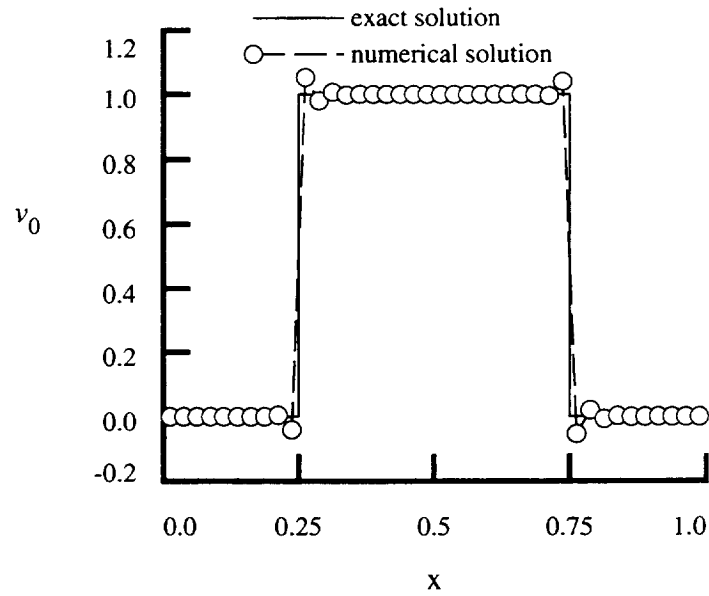


Figure 6. Solution of linear problem after one time period, produced by DG method with $p = 6$.

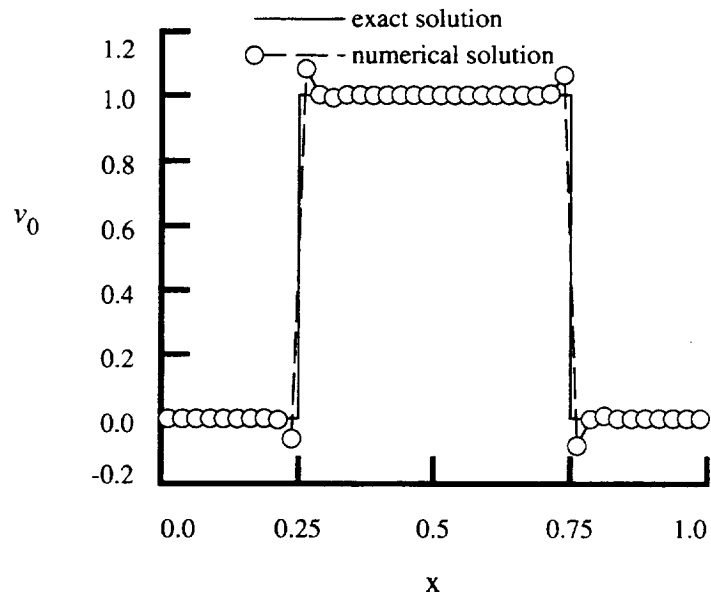


Figure 7. Solution of linear problem after five time periods, produced by DG method with $p = 6$.

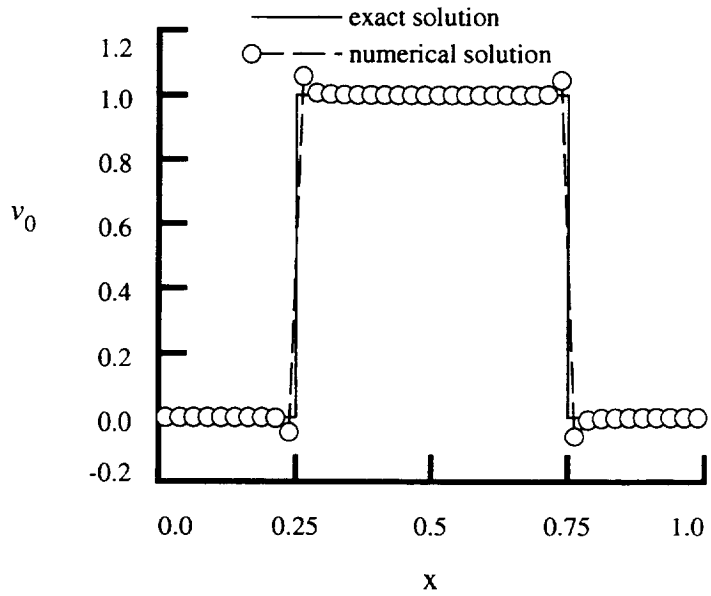


Figure 8. Solution of linear problem after 50 time periods, produced by DG method with $p = 6$.

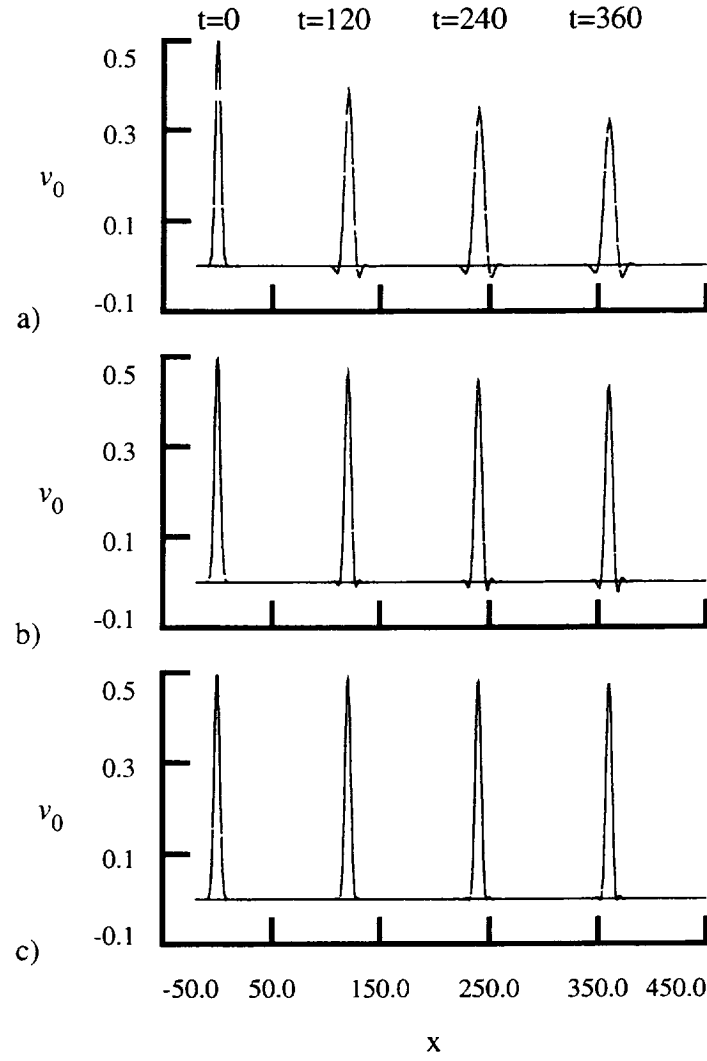


Figure 9. DG method applied to advection of Gaussian pulse. a) $p = 1$ with 235 elements. b) $p = 2$ with 156 elements. c) $p = 3$ with 117 elements.

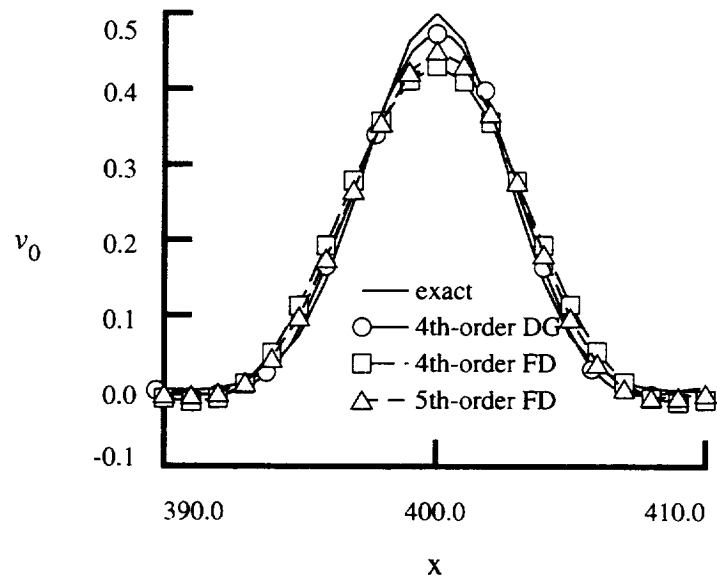


Figure 10. Comparison of fourth-order DG method with fourth- and fifth-order finite-difference (FD) method.

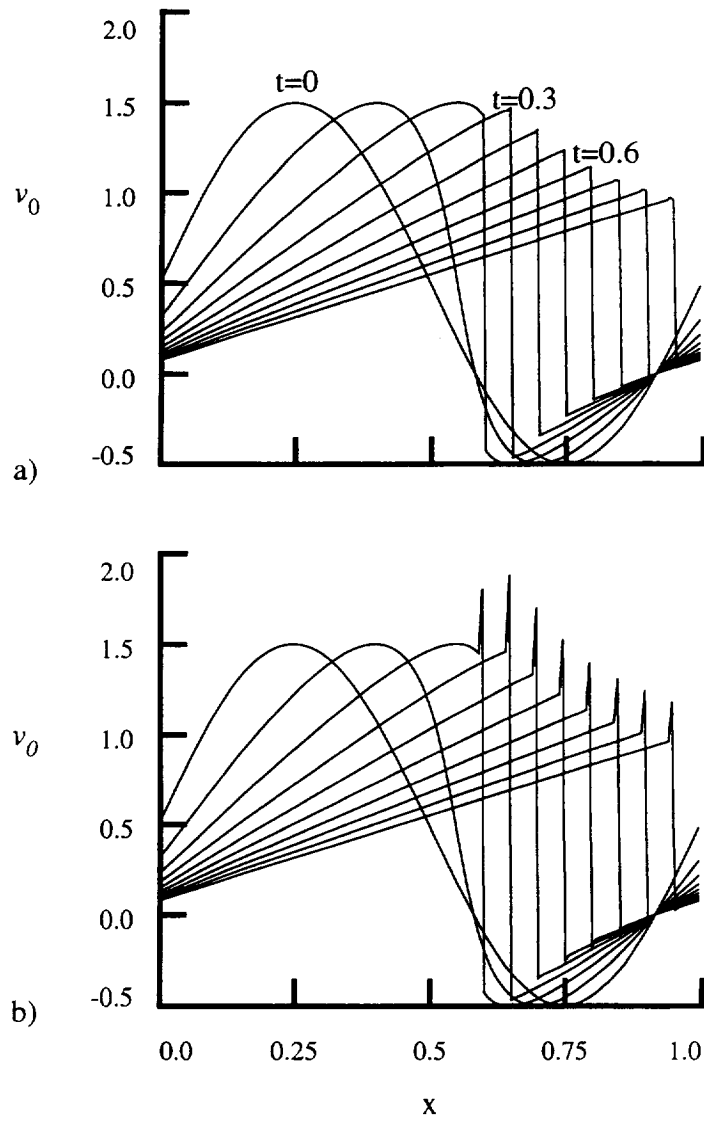


Figure 11. Solution of nonlinear equation. a) $p = 1$. b) $p = 2$.

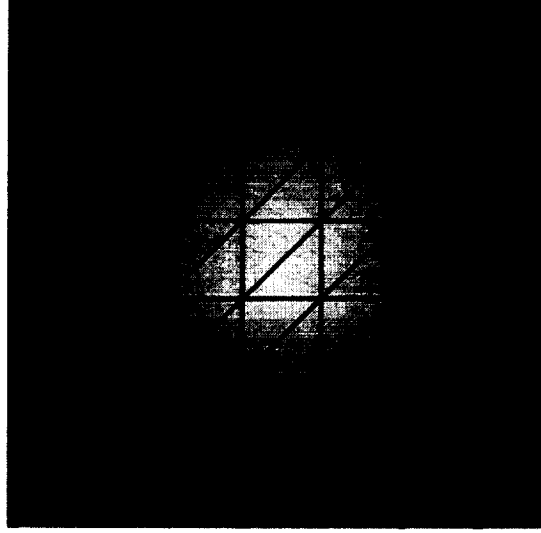


Figure 12. Triangulated grid and solution of scalar advection problem.

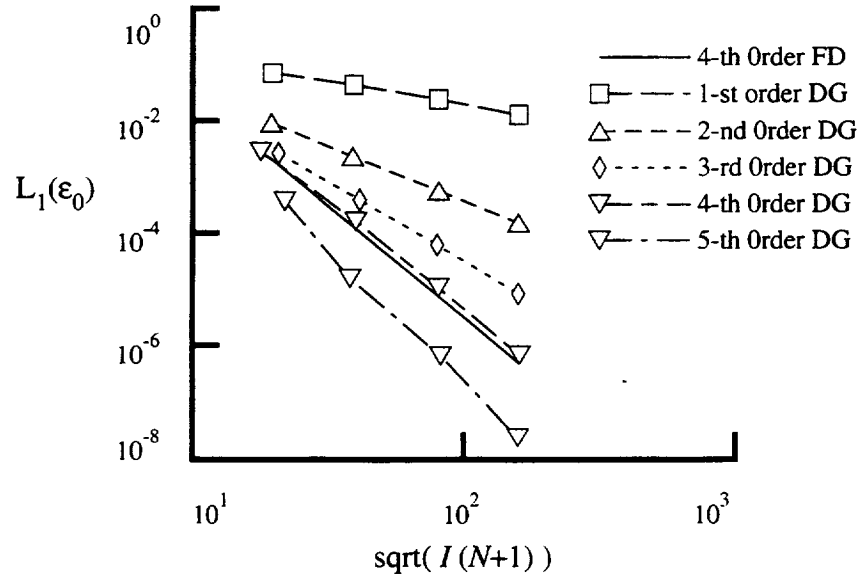


Figure 13. Convergence of solution for scalar advection on unstructured grid for various orders of accuracy.

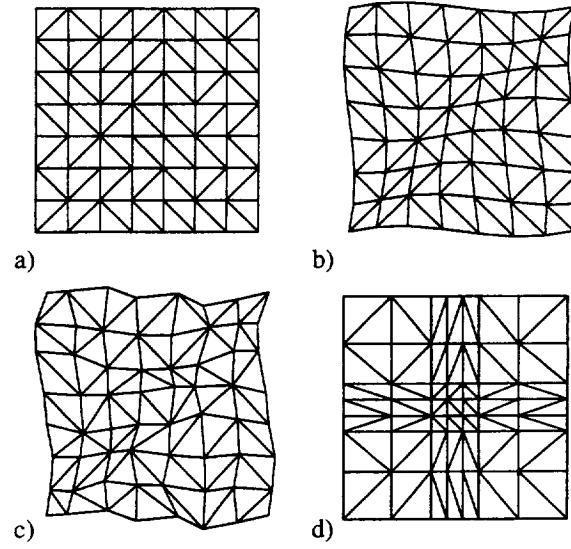


Figure 14. Variation on baseline unstructured grid. a) Grid A, Random triangulation. b) Grid B, Smoothly clustered toward diagonal. c) Grid C, Random perturbation of 20 percent of the mean cell spacing. d) Grid D, Discontinuous mesh variation.

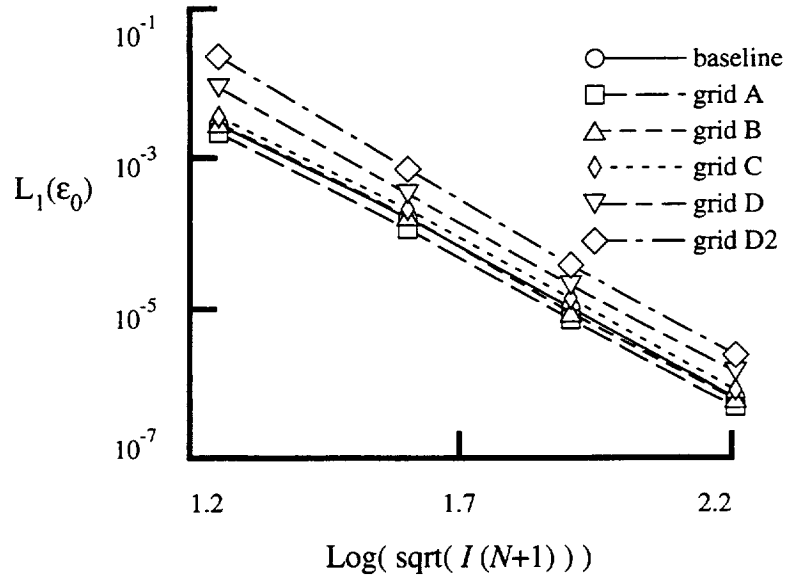


Figure 15. Convergence of solution for scalar advection for fourth-order method on variations of baseline unstructured grid.

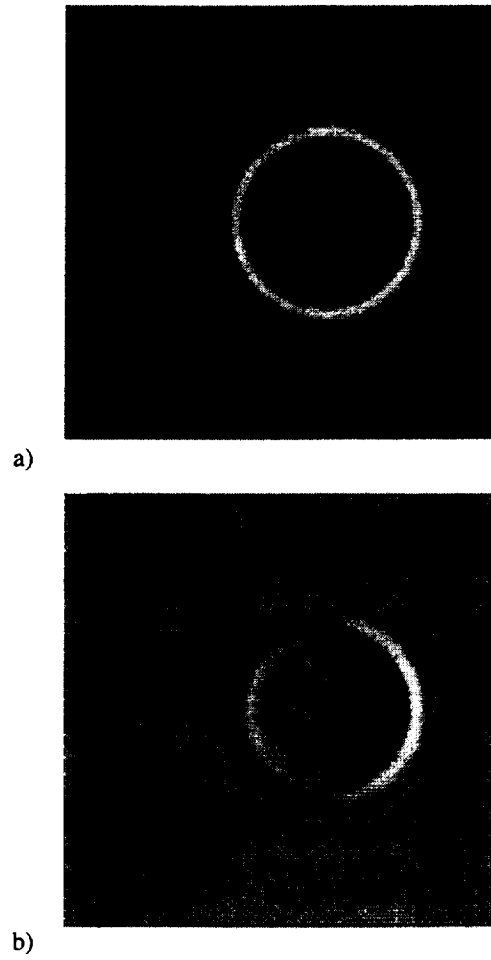


Figure 16. Acoustic wave modeled by linear Euler equations: $p = 3$ and $t = 40$. a) P . b) u .

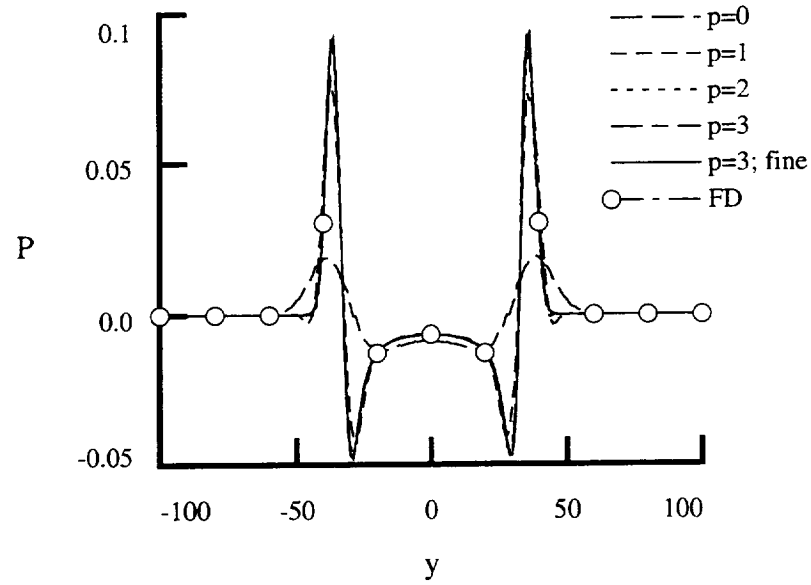


Figure 17. Solution of linear Euler equations: pressure on $x = 0$ at $t = 40$.

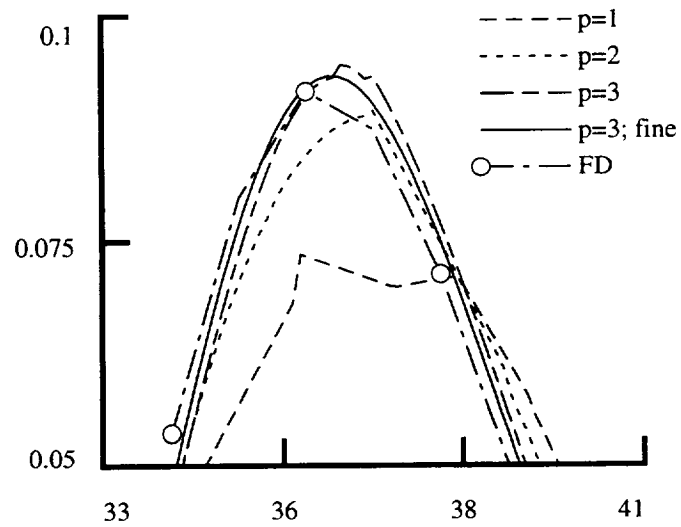


Figure 18. Solution of linear Euler equations: enlargement of pressure near $y = 36$ on $x = 0$ at $t = 40$.

REPORT DOCUMENTATION PAGE			Form Approved OMB No. 0704-0188	
Public reporting burden for this collection of information is estimated to average 1 hour per response, including the time for reviewing instructions, searching existing data sources, gathering and maintaining the data needed, and completing and reviewing the collection of information. Send comments regarding this burden estimate or any other aspect of this collection of information, including suggestions for reducing this burden, to Washington Headquarters Services, Directorate for Information Operations and Reports, 1215 Jefferson Davis Highway, Suite 1204, Arlington, VA 22202-4302, and to the Office of Management and Budget, Paperwork Reduction Project (0704-0188), Washington, DC 20503.				
1. AGENCY USE ONLY(Leave blank)	2. REPORT DATE August 1996	3. REPORT TYPE AND DATES COVERED Contractor Report		
4. TITLE AND SUBTITLE QUADRATURE-FREE IMPLEMENTATION OF DISCONTINUOUS GALERKIN METHOD FOR HYPERBOLIC EQUATIONS		5. FUNDING NUMBERS C NAS1-19480 WU 505-90-52-01		
6. AUTHOR(S) H. L. Atkins Chi-Wang Shu				
7. PERFORMING ORGANIZATION NAME(S) AND ADDRESS(ES) Institute for Computer Applications in Science and Engineering Mail Stop 132C, NASA Langley Research Center Hampton, VA 23681-0001		8. PERFORMING ORGANIZATION REPORT NUMBER ICASE Report No. 96-51		
9. SPONSORING/MONITORING AGENCY NAME(S) AND ADDRESS(ES) National Aeronautics and Space Administration Langley Research Center Hampton, VA 23681-0001		10. SPONSORING/MONITORING AGENCY REPORT NUMBER NASA CR-201594 ICASE Report No. 96-51		
11. SUPPLEMENTARY NOTES Langley Technical Monitor: Dennis M. Bushnell Final Report Presented at the 2nd AIAA/CEAS Aeroacoustics Conference; Submitted to the AIAA Journal.				
12a. DISTRIBUTION/AVAILABILITY STATEMENT Unclassified-Unlimited Subject Category 64		12b. DISTRIBUTION CODE		
13. ABSTRACT (Maximum 200 words) A discontinuous Galerkin formulation that avoids the use of discrete quadrature formulas is described and applied to linear and nonlinear test problems in one and two space dimensions. This approach requires less computational time and storage than conventional implementations but preserves the compactness and robustness inherent in the discontinuous Galerkin method. Test problems include the linear and nonlinear one-dimensional scalar advection of smooth initial value problems that are discretized by using unstructured grids with varying degrees of smoothness and regularity, and two-dimensional linear Euler solutions on unstructured grids.				
14. SUBJECT TERMS discontinuous Galerkin; quadrature free integration; high order; stability; Euler; unsteady; time accurate			15. NUMBER OF PAGES 35	
			16. PRICE CODE A03	
17. SECURITY CLASSIFICATION OF REPORT Unclassified	18. SECURITY CLASSIFICATION OF THIS PAGE Unclassified	19. SECURITY CLASSIFICATION OF ABSTRACT	20. LIMITATION OF ABSTRACT	